



Droplet and slug formation in polymer electrolyte membrane fuel cell flow channels: The role of interfacial forces

Carlos E. Colosqui^{a,*}, May J. Cheah^a, Ioannis G. Kevrekidis^{a,b}, Jay B. Benziger^{a,**}

^a Department of Chemical and Biological Engineering, Princeton University, Princeton, NJ 08544, USA

^b Program in Applied and Computational Mathematics, Princeton University, Princeton, NJ 08544, USA

ARTICLE INFO

Article history:

Received 18 July 2011

Received in revised form 19 August 2011

Accepted 20 August 2011

Available online 26 August 2011

Keywords:

PEM fuel cell

Two-phase flow

Slug flow

Water management

Pressure drop

ABSTRACT

A microfluidic device is employed to emulate water droplet emergence from a porous electrode and slug formation in the gas flow channel of a PEM fuel cell. Liquid water emerges from a 50 μm pore forming a droplet; the droplet grows to span the entire cross-section of a microchannel and transitions into a slug which detaches and is swept downstream. Droplet growth, slug formation, detachment, and motion are analyzed using high-speed video images and pressure–time traces. Slug volume is controlled primarily by channel geometry, interfacial forces, and gravity. As water slugs move downstream, they leave residual micro-droplets that act as nucleation sites for the next droplet-to-slug transition. Residual liquid in the form of micro-droplets results in a significant decrease in slug volume between the very first slug formed in an initially dry channel and the ultimate “steady-state” slug. A physics-based model is presented to predict slug volumes and pressure drops for slug detachment and motion.

© 2011 Elsevier B.V. All rights reserved.

1. Introduction

Electrochemical conversion systems have garnered increasing interest as an economically viable solution in the strategic shift towards sustainability and clean energy production. Polymer electrolyte membrane (PEM) fuel cells, in particular, are favored for both stationary (e.g. off-grid electricity production) and mobile applications (e.g. automotive transportation) due to their ability to operate at relatively low temperatures and zero point of use emissions [1].

A major challenge for optimal and stable operation of PEM fuel cell has been the management of the liquid water produced. While a well-hydrated PEM is necessary for high proton conductivity [2], the accumulation of water can cause deterioration of the fuel cell performance. Liquid water can flood the gas flow channels, hindering the transport of gaseous reactants. Extensive effort is being directed towards optimizing water removal techniques. The conventional approach to enhance water removal is to increase gas flow rates with the expectation that the large fluid shear forces will detach and eject liquid water in the form of droplets [3–5]. However, this strategy leads to low reactant consumption, dehydration of the polymeric membrane, and parasitic losses from air

compression and humidification of the air stream (to rehydrate the membrane) [6,7]. To improve the system efficiency we must understand the hydrodynamics of gas–liquid flow so as to minimize the energy required for water removal.

A comprehensive review of two-phase flow in gas channels of PEM fuel cells was published in 2010 [8]. Experimental studies of the multiphase flow in fuel cell channels have been performed *in situ* (i.e. within an operational fuel cell) and *ex situ* (e.g. using microfluidic devices). The *in situ* study by Hussaini and Wang showed that at moderate-to-high gas flow rates, water can be removed as a mist [9]. Droplets coalesced towards the outlet of the fuel cell [4,10] and/or at the bends of serpentine flow channels [11,12]. After coalescence, mist flow transitioned into film/annular flow or slug flow. Film flow typically occurs at the corners of the gas flow channels and can transition to slug flow if the film grows to a critical thickness [13]. *Ex situ* studies permit analysis of the two-phase flow at specific flow regimes determined by gas and liquid flow rates (conditions do not vary along the flow channel). Lu et al. employed a microfluidic cell and reported slug flow, film flow, and mist flow depending on the gas and liquid flow rates, channel surface wettability, geometry and orientation [5,14]. Bazylak et al. [15] focused on the mist flow to slug flow transition at moderate gas flow rates while Theodorakakos et al. [16] focused on the mechanism of droplet detachment at high gas flow rates. Steinbrenner et al. reported the general evolution of flow regimes for different porous electrode wettability [17]. In both *in situ* and *ex situ* studies, the pressure drop in the flow channel has been identified as an important diagnostic tool. Trabold [18] showed that the pressure

* Corresponding author. Tel.: +1 609 258 2977; fax: +1 609 258 0211.

** Corresponding author. Tel.: +1 609 258 5416; fax: +1 609 258 0211.

E-mail addresses: colosqui@princeton.edu (C.E. Colosqui), benziger@princeton.edu (J.B. Benziger).

drop is a sensitive indicator of water slugs in the flow channel. More recently, the pressure drop has been correlated with different flow topologies [19] and fuel cell performance [20,21]. Anderson et al. also reviewed numerical simulations on the two-phase flow in the gas flow channels of PEM fuel cells [8]. A couple of the numerical studies have focused on understanding the dynamics of droplet detachment from the porous electrode surface [16,22,23]. In these studies, the porous electrode wettability, and gas and liquid flow rates were varied to explore the effect of these parameters on the droplet behavior.

PEM fuel cells utilize different flow field configurations (such as serpentine, parallel, or interdigitated microchannels) where the magnitude of fluid shear forces can differ by orders of magnitude. Furthermore, the surfaces of the gas channel commonly exhibit nontrivial wetting properties due to their irregular topology (e.g. porous electrode) and chemical treatment (e.g. hydrophobic coatings). The complexity of the overall system obscures the fundamental physical phenomena making it difficult to quantify the observed flow dynamics.

The goal of the present study is to better understand the dynamics of droplet growth, slug formation, and the development of films. Droplets that elongate over the length of the channel without forming a slug is what we refer to as films in this study. For the purpose of this study we employ a well-defined geometry where the magnitude of interfacial, hydrodynamic, and gravity effects can be readily quantified. We employed a transparent channel with a 1.6 mm × 1.6 mm cross section and a single 50 μm pore, typical of the largest pores observed in commercial gas diffusion layers (GDLs), from which liquid water emerges [24]. The gas flow channel is oriented in two different horizontal configurations in which gravity either hinders or assists the emergence of liquid into the channel and the ensuing formation of slugs. The simplicity of the experimental setup provides quantitative measurements of droplet and slug volumes, and the forces required for slug detachment and motion.

Previous work by our group [25] examined water transport in single-channel fuel cells. Key points from that study are: (1) the water produced emerges into the gas channels *through the largest pores* of the (hydrophobic) GDL; (2) liquid slugs form directly from growing droplets and aggregation of residual liquid in the channel; (3) the orientation of the channel with respect to gravity significantly affects the flow topology and liquid distribution; and (4) different flow topologies (e.g. slugs and films) can occur for the same gas feed rates. This study also reported large spatio-temporal current fluctuations resulting from the formation and motion of liquid films and slugs.

The paper is structured as follows: (Section 2) the gas flow regimes relevant to the cathode gas flow channels are identified; (Section 3) the experimental system combining visualization with pressure measurements is described; (Section 4) the correlation of pressure–time traces and video images is presented to describe the sequence of droplet growth, slug formation, detachment and motion; (Section 5) the results of slug volume, pressure to detach slugs, and pressure to move slugs are summarized as functions of gas and liquid flow rates and channel orientation; (Section 6) physical models are presented to predict slug volumes and pressure drops to detach and move slugs; (Section 7) we comment on implications for fuel cell design; and (Section 8) final conclusions are drawn.

2. Gas flow regimes in PEM fuel cells

The volumetric flow rate of gaseous reactants to a fuel cell is determined by the integrated current density j over the active area A_{FC} of the fuel cell. However, the flow field design, i.e. arrangement

Table 1

Reynolds numbers for air flow in the cathode of a single serpentine channel, Re_{SC} , and for multiple parallel channels, Re_{MC} , with stoichiometric coefficient $\epsilon = 2.0$. The studied experimental conditions correspond to Reynolds numbers between 2 and 25 which are commonly observed for fuel cells with multiple parallel channels.

A_{FC} (cm ²)	j (A cm ⁻²)	Re_{SC}	Re_{MC}
10	0.1	35	2.4
10	1.0	350	24
100	0.1	350	7.6
100	1.0	3500	76
1000	0.1	3500	24
1000	1.0	35,000	240

of flow channels (see Fig. 1) and channel geometry, will dictate the gas velocities and thus the flow regimes at a given current density which prescribes the liquid flow rate.

The Reynolds number is useful to characterize the flow regimes in the gas flow channels of fuel cells. Assuming that the gas channels have a square cross-section of width W , the (gas-phase based) Reynolds number for a single channel (SC) serpentine flow (shown in Fig. 1a) is

$$Re_{SC} = \frac{\epsilon}{y_{O_2}} \frac{j}{4\mathcal{F}} \frac{M_w}{W\mu_G} A_{FC}. \quad (1)$$

For multiple channels (MC), such as the parallel flow channels illustrated in Fig. 1b, assuming the channel width W and rib width W_L are equal we find that the number of channels is $N_{channel} = \sqrt{A_{FC}/2W}$ and thus

$$Re_{MC} = \frac{\epsilon}{y_{O_2}} \frac{j}{2\mathcal{F}} \frac{M_w}{\mu_G} \sqrt{A_{FC}}. \quad (2)$$

Above, ϵ is the stoichiometry of the cathode feed (oxygen molar flow/Faradaic oxygen molar flow at a given current), y_{O_2} is the mole fraction of the feed ($y_{O_2} = 1$ for pure oxygen and $y_{O_2} = 0.2$ for air), A_{FC} is the fuel-cell area, $\mathcal{F} = 96,485 \text{ C mol}^{-1}$ is the Faraday constant, M_w is the molecular weight of the gas ($M_w = 32 \text{ g mol}^{-1}$ for pure oxygen, and $M_w = 29 \text{ g mol}^{-1}$ for air), and μ_G is the dynamic viscosity of the gas ($\mu_G = 2.018 \times 10^{-5} \text{ kg m}^{-1} \text{ s}^{-1}$ for pure oxygen, $\mu_G = 1.985 \times 10^{-5} \text{ kg m}^{-1} \text{ s}^{-1}$ for air at 20 °C).

Table 1 summarizes representative Reynolds numbers for the single serpentine channel, Re_{SC} , and for the multiple parallel channel, Re_{MC} , flow configurations for different fuel-cell areas, A_{FC} , and current densities, j . Reynolds numbers for the multiple parallel channels are smaller than those for the single serpentine channel flow field. The experiments we will present here focus on laminar flow conditions ($Re < 100$). Laminar flow conditions are encountered in fuel cells with multiple parallel flow channels and small-area fuel cells with a single serpentine flow channel.

3. Experimental setup

The experimental apparatus (Fig. 2) consisted of a custom-built microfluidic cell, a mass flow controller, a syringe pump, and a pressure transducer. Experimental conditions and physical parameters are summarized in Table 2. Each microfluidic cell is comprised of two machined acrylic sheets bolted together to form a transparent straight microchannel with square cross section. The height and width of the channel are $H = W = 1.6 \text{ mm}$. The length of the microchannel is 125 mm ($L_c = 80H$). The microchannels have a 50 μm pore (liquid inlet) centered in one channel wall and placed 100 mm away from the exit of the channel. The working fluids are nitrogen gas and liquid water at room temperature. A constant volumetric flow rate of nitrogen gas Q_G is delivered through a mass flow controller while a constant liquid water volumetric flow rate Q_L is supplied by a syringe pump. Gas flows ranged from $Q_G = 3\text{--}21 \text{ mL min}^{-1}$ and liquid flows ranged from

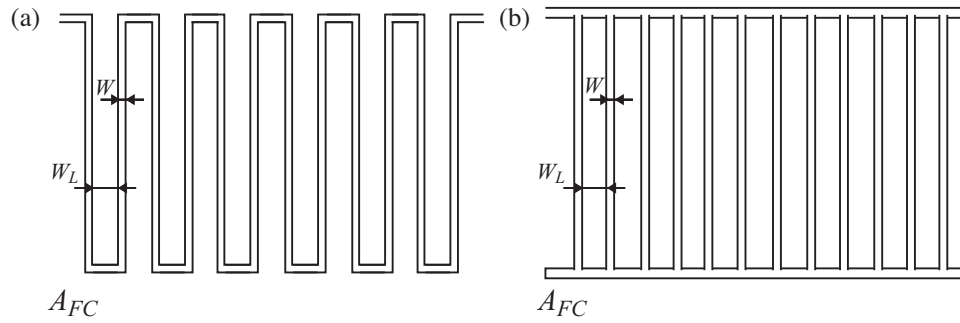


Fig. 1. Common flow field designs in PEM fuel cells. (a) Single serpentine gas channel. (b) Multiple parallel gas channels.

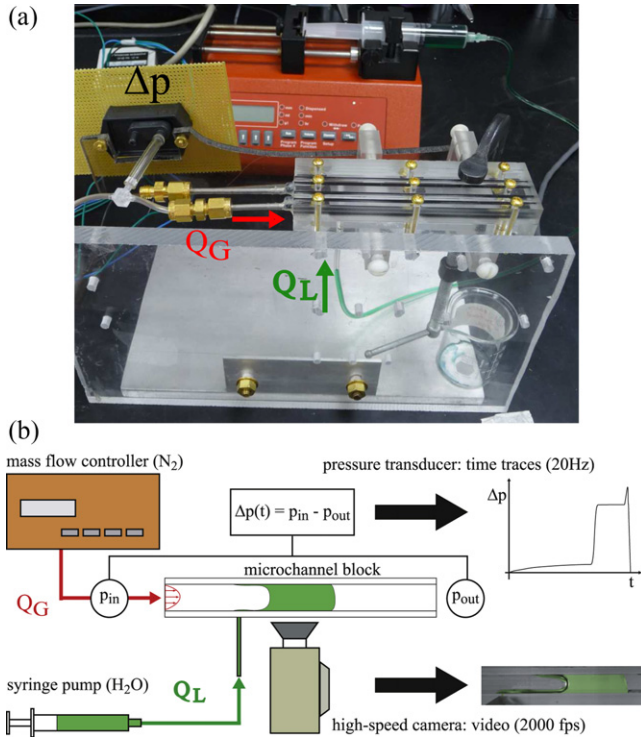


Fig. 2. Experimental apparatus. (a) Photograph and (b) schematic.

Table 2

Experimental conditions and physical parameters adopted.

Channel length	$L = 101.6 \text{ mm}$
Channel height	$H = 1.6 \text{ mm}$
Channel width	$W = 1.6 \text{ mm}$
Pore diameter	$d = 50 \text{ }\mu\text{m}$
Gas volume rate	$Q_G = 3\text{--}21 \text{ mL min}^{-1}$
Liquid volume rate	$Q_L = 5\text{--}75 \text{ }\mu\text{L min}^{-1}$
Gas density	$\rho_G = 1.2 \text{ kg m}^{-3}$
Liquid density	$\rho_L = 997 \text{ kg m}^{-3}$
Gas viscosity	$\mu_G = 1.7 \times 10^{-5} \text{ N s m}^{-2}$
Liquid viscosity	$\mu_L = 1.0 \times 10^{-3} \text{ N s m}^{-2}$
Surface tension	$\gamma = 0.072 \text{ N m}^{-1}$
Capillary pressure	$p_{cap} = \gamma/H = 46.0 \text{ N m}^{-2}$
Nominal speed	$U = Q_G/H^2 = 2\text{--}14 \times 10^{-2} \text{ m s}^{-1}$

$Q_L = 5\text{--}75 \text{ }\mu\text{L min}^{-1}$. Gas and liquid flow rates were chosen so that at “steady” state, each slug exited the gas flow channel before the next droplet grew to significant size. The liquid flow rates employed would correspond to a maximum current density of 1.3 A cm^{-2} for a fuel cell with an active area of 10 cm^2 .

For the present experiments, the microchannel is oriented in two horizontal configurations with the gravity field perpendicular

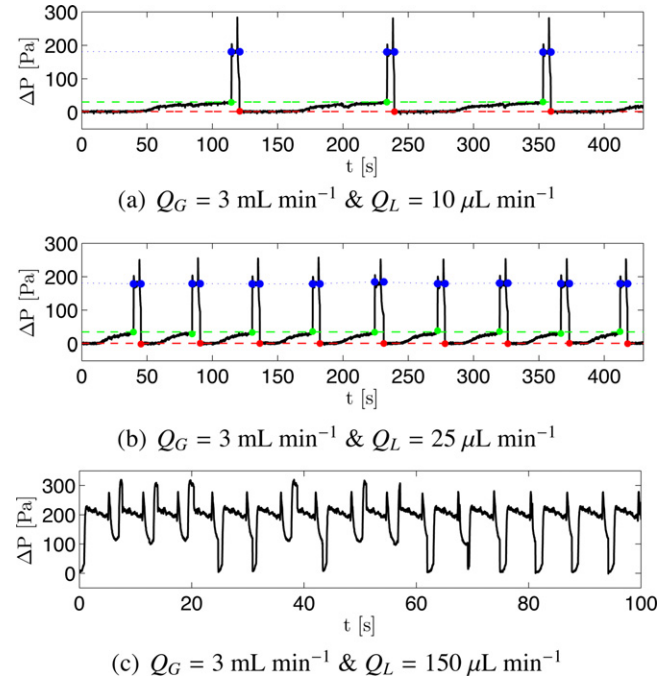


Fig. 3. Pressure–time traces acquired by the transducer and processed with MATLAB™. The effect of varying Q_L is reflected in the time scales for slug formation and slug flow. (a)–(b) Single-slug flow ($5 \leq Q_L \leq 75 \text{ }\mu\text{L min}^{-1}$) and stationary “dripping” reached by following the experimental protocol; green dots: channel bridging/slug formation; blue dots: slug flow; red dots: slug ejection. (c) Multiple-slug flow occurs when Q_L is increased beyond the above flow range. (For interpretation of the references to color in this figure legend, the reader is referred to the web version of this article.)

to the gas stream. (a) Pore-up or sessile droplet configuration where gravity acts against the liquid flow emerging from the pore ($g < 0$). (b) Pore-down or pendant droplet configuration where gravity acts with the liquid flow emerging from the pore ($g > 0$).

A low-pressure transducer (Omega PX-160) was employed to acquire differential pressure $\Delta p = p_{in} - p_{out}$ between the channel inlet pressure, p_{in} , and outlet pressure, p_{outlet} . The measurement range of the pressure transducer is 0–250 (gauge) Pa, with an accuracy of ± 2.5 Pa. The differential pressure was sampled at a frequency of 20 Hz. A set of typical pressure–time traces acquired by the transducer is shown in Fig. 3. The formation time of a water slug depends primarily on the liquid flow rate Q_L , while the time for a slug to be removed from the channel depends primarily on the gas flow rate Q_G . At a fixed Q_G and at sufficiently low Q_L , we observe single slugs in the channel and the differential inlet pressure returns to baseline level shortly after each slug exits the channel (see Fig. 3a and b). At high Q_L , a second slug forms before the previous slug exits the channel. The pressure–time trace becomes more complex due

to the pressure drops associated with each droplet/slug, as seen in Fig. 3c. The maximum values observed for the differential pressure for multiple slugs are still comparable to the those observed for single slugs.

We developed a MATLABTM script to locate points in the pressure cycle corresponding to the droplet-to-slug transition and to the endpoints of slug flow. These points, illustrated in see Fig. 3a and b, correspond to time instances where the magnitude of the time derivative of the differential pressure climbs above given threshold values that were heuristically determined for each flow condition.

The process of slug formation and detachment was recorded using a high-speed camera (Phantom V5, Vision Research Inc.) at a frame rate of 2000 fps.

In order to characterize wetting properties (e.g. interfacial forces, contact angle hysteresis) of the acrylic material employed in the micro-fluidic cells, static (advancing/receding) contact angles for air–water were determined by Wilhelmy plate measurements. Smooth and sanded (to simulate machined surfaces) acrylic sheets were tested with the first submersion dry and the second submersion pre-wetted. Whether dry or pre-wetted, the smooth acrylic sheet had advancing and receding contact angles of 84° and 55° respectively. Dry sanded acrylic sheets had advancing contact angles of 100°. Pre-wetted sanded acrylic sheets had advancing contact angles that varied between 40° and 100°; the angle decreased with increasing surface roughness. In both dry and pre-wetted conditions, the sanded acrylic sheet had receding angles that varied between of 25° and 37°. The measured values of the static contact angles are needed as input parameter for the predictive models presented in Section 6.

In a fuel cell, the physical and chemical treatments, and the complex topology of channel and GDL surfaces produce a wide range of contact angles that is difficult to characterize. The present experimental setup is designed to reproduce the fundamental phenomena of droplet growth and slug formation observed in previous *in situ* studies by our group [25]. Despite the simple studied system, the experimental results are highly sensitive to the past history of conditions in the flow channel. It could take several hours after starting the gas and liquid flows for steady-state formation of slugs to be established. In order to improve reproducibility, a fixed experimental protocol was employed: (1) the micro-channel was completely dried with a high flow rate of dry nitrogen gas; (2) gas and liquid flows were initiated; and (3) steady state was achieved after circa 20 consecutive slugs with size fluctuations <10% have formed and exited the channel. This experimental protocol ensured that similar wetting conditions are achieved at a particular gas–liquid flow combination. All experimental data presented in this work are recorded after the cyclic pressure variation becomes stationary. Under such conditions, the system exhibits a characteristic “dripping period” T_F , which is the elapsed time between consecutive slug evacuations from the channel as seen in Fig. 3a and b.

4. Experimental observations: slug formation, detachment, and removal

In the range of $Re_G < 25$ we always observed slug flow at “steady” state. The formation and removal of the slugs always went through the same well-defined sequence of steps, which are depicted in Figs. 4 and 5. Fig. 4 shows the pressure–time trace along with selected (side view) video images for the droplet growth, slug formation, slug detachment, and slug removal. Fig. 5 shows the schematic of the three dimensional droplet and slug formation. The

liquid phase adopts four basic topological structures shown in Fig. 5. These structures are referred to as:

- (I) Sessile or pendant droplets. These form at the site of the emergent pore and only contact the channel wall (top or bottom) from which the droplet emerges.
- (II) Laterally confined droplets. As the sessile or pendant droplets grow, they span the channel side to side without touching the wall opposite the emergent pore. The laterally confined droplets are nearly symmetric, with the receding side of the confined droplet pinned at the emergent pore. As the laterally confined droplets grow, they appear as hemispherical caps from the side as seen in Fig. 4b–d.
- (III) Fully confined droplets. The laterally confined droplets first touch the wall opposite the emergent pore at the channel corners. The droplet then spreads longitudinally, while apparently remaining pinned laterally at the corners. The receding end of the droplet is pinned at the emergent pore. A gap is formed, between the droplet and the opposing wall, through which gas still flows; this gap is illustrated in Fig. 5d. Viewed from the side, these fully confined droplets are no longer front-back symmetric. The apparent advancing contact angle increases; this can be seen in Fig. 4e and f and values for the contact angles are summarized in the table in Fig. 4.
- (IV) Slugs. After growing to a certain length the gap between the fully confined droplet and its opposing wall collapses and the water completely spans the gas flow channel forming a slug (Fig. 4g). When the gas flow is thus blocked, the upstream gas pressure increases causing the slug to detach and move down the channel. As the slug begins to move, the advancing contact angle approaches 90° while the receding contact angle approaches 0° as seen in Figs. 4(h and i) and 5e.

Steps I–IV are well-defined in the pressure–time trace shown in Figs. 4a and 5a. Slug formation and detachment is evidenced by a rapid increase in the differential pressure between time instances t_1 and t_2 . The pressure stays high, pushing the slug along the length of the gas flow channel between time instances t_2 and t_3 . The mean pressure for slug motion ($t_2 < t < t_3$), obtained by averaging several cycles, is considered constant as illustrated in Fig. 5a. At $t = t_3$ there is a modest increase in the differential pressure as the slug is expelled from the end of the channel. After the slug is expelled, the pressure drops back to baseline level. The next droplet starts to form the moment the slug detaches (time instance t_2) and continues to grow while the slug is pushed down the channel and expelled.

The frequency of slug formation is dependent on the gas and liquid flow rates; however, the size of the slugs and the pressure required for slug detachment and motion exhibits minimal dependence on the gas and liquid flow rates. The sudden transition from fully confined droplets to slugs occurs over a millisecond time scale, and produces regular sized slugs. Within a given experimental run, after “steady” state is achieved, slug volumes are constant. The droplet-to-slug transition appears to nucleate near the advancing end of the fully confined droplet at a channel corner. The nucleation frequently occurs where residual micro-droplets were left behind by the previous slugs. A thin film of water in the corners of the channel can be seen in the photo sequence of Fig. 4. Dark lines that delineate the channel are evident downstream of the emergent pore and are absent upstream. Those dark lines are the result of a thin film of water left behind from the previous ejected slug. The deposition of such thin films is common in coating flows (e.g. Landau–Levich flows). The film causes the receding contact angle to vanish ($\theta_R \sim 0^\circ$) while the advancing contact angle is large, ($\theta_A \sim 90^\circ$).

¹ measurements available at <http://pemfc.princeton.edu/PEMFC.data.html>.

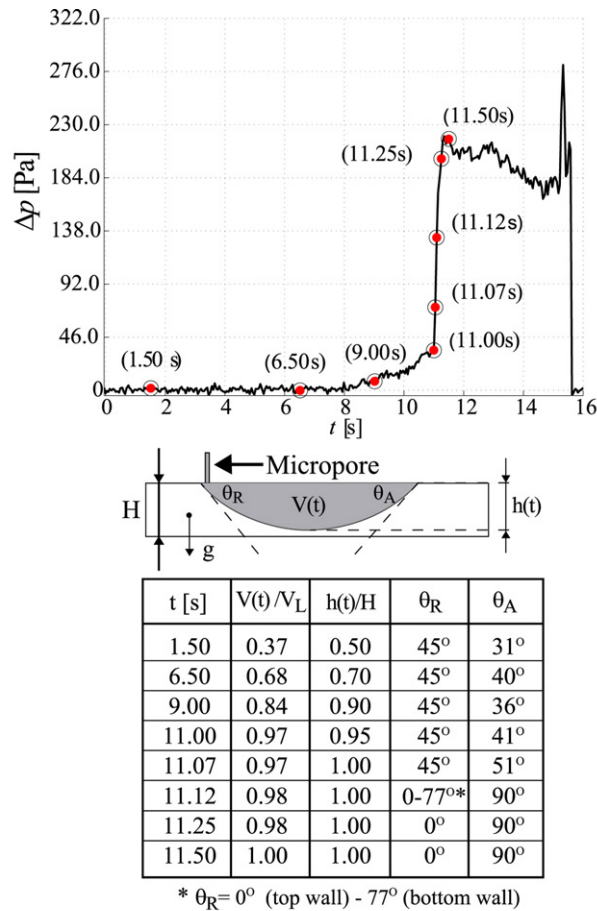
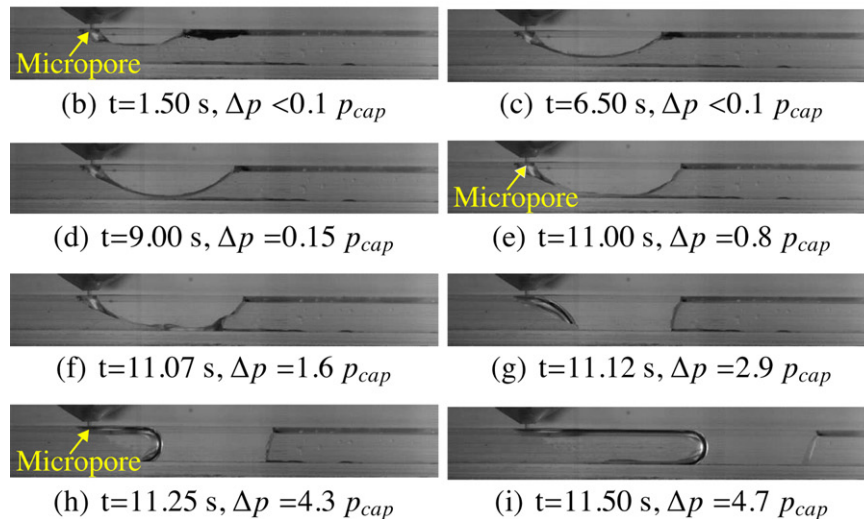
(a) Δp vs. t and geometric configuration

Fig. 4. Correlation of pressure–time trace and high-speed video images (pendant droplet). (a) Pressure–time trace and tabulated data: $Q_C = 3 \text{ mL min}^{-1}$; $Q_L = 50 \text{ } \mu\text{L min}^{-1}$; $p_{cap} = \gamma/H = 46 \text{ N m}^{-2}$; slug volume $V_L \simeq 13 \text{ } \mu\text{L}$. (b–i) High-speed video images (2000 fps): side view.

5. Experimental results

The basic mechanism of slug formation and removal is the same, independent of gas and liquid flow rates and up/down orientation. To quantify and compare the volumes of slugs and the forces required to remove them, pressure–time traces are recorded for different gas–liquid flow rates and pore orientations. From these pressure–time traces we extracted four key observables:

time elapsed for slug formation, $t_F = t_4 - t_0$; pressure difference at the droplet-to-slug transition (i.e. bridge pressure), $\Delta p_1 = p_1 - p_{out}$; transit time for the slug to be ejected, $t_T = t_3 - t_2$; and pressure difference required to push the slug down the gas flow channel, $\Delta p_2 = p_2 - p_{out}$. About 20–50 pressure–time traces for each experimental condition were analyzed to determine mean values and standard deviations for the observables. On any day the steady-state values for the slug volume and pressure drops to move the

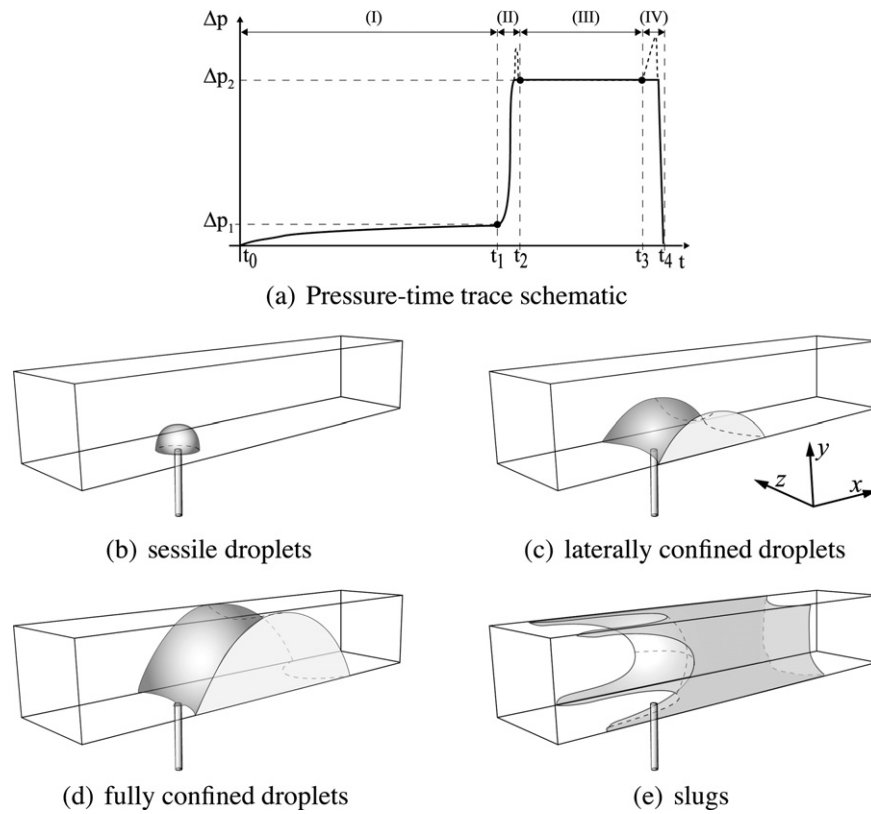


Fig. 5. Droplet and slug formation. (a) Stages in the pressure–time trace: (I) formation ($t_0 \leq t < t_1$); (II) droplet-to-slug transition ($t_1 \leq t < t_2$); (III) slug flow ($t_2 \leq t < t_3$); and (IV) ejection ($t_3 \leq t < t_4$). Liquid-phase 3D topologies for sessile or pendant droplet configurations: (b) small droplets ($t \simeq t_0$); (c) laterally confined droplets ($t_0 < t < t_1$); (d) fully confined droplets ($t \simeq t_1$); and (e) slugs ($t_3 < t < t_4$).

slugs were highly reproducible over periods of tens of minutes, with standard deviations of <5% of the measured values. However, reproducing the same experimental conditions from day to day can result in slug volumes that are substantially different. We attribute these large day-to-day fluctuations to differences in how residual water films aggregate at the corners of the gas flow channel. We performed repeated runs for a limited set of experimental conditions; the reported error bars represent day-to-day reproducibility.

5.1. Slug volumes

The time elapsed between consecutive slug detachments is the slug formation time $t_F = t_4 - t_0$. This period ranges from 10 to 300 s; it decreases with increasing liquid flow rate, Q_L , and increases slightly with increasing gas flow rate Q_G . Slug volumes $V_L = Q_L t_F$ as functions of gas and liquid flow rates and pore orientation are shown in Fig. 6. With the pore in the up orientation, sessile droplets form and the sessile slug volumes are scattered between 3 and 5 H^3 (see Fig. 6a). For convenience we will use the terms “sessile slug” and “pendant slug” in referring to slugs that derived from sessile or pendant droplets. There was no discernible trend in slug volume V_L with liquid flow rate; and V_L decreases by a small amount with increased gas flow rate. The slug volumes are distinctly smaller when the pore is in the down orientation, forming pendant droplets and slugs; pendant slug volumes are 1–2 H^3 (see Fig. 6b) and the scatter of the pendant slug volumes due to changes of gas and liquid flow rates is much smaller than that for sessile slugs.

5.2. Effect of gravity and surface wetting on slug volume

To gain a better understanding of the roles of gravity and residual water on the channel walls, single-slug formation with no gas

flow was first studied. Two sets of experiments were performed, corresponding to the slug formation in a dry channel and in a pre-wetted channel. The channel was dried by flowing dry nitrogen for about 10 min. Water was injected through the pore at rates of 5–75 $\mu\text{L min}^{-1}$ and the growth of a single droplet and the droplet-to-slug transition was recorded by video. The side views of the pendant and sessile droplets just before the conversion to a slug are shown in Fig. 7. Immediately after the droplet-to-slug transition occurs the liquid injection is stopped to prevent the slug from filling the entire channel; the formed slug was then removed by flowing 5 cm^3 of nitrogen. A second droplet was formed to compare pre-wetted channel conditions against dry channel conditions. Fig. 7a and c shows that, in a dry channel, sessile droplets can form slugs that are approximately 50% larger than slugs derived from pendant droplets. In the dry channel, the advancing contact angle is approximately 90° for sessile droplets (Fig. 7a) and 110° for pendant droplets (Fig. 7c). After the channel walls are pre-wetted, the contact angles are reduced to $\sim 45^\circ$ for both sessile (Fig. 7b) and pendant droplets (Fig. 7d). At the droplet-to-slug transition, droplets in a pre-wetted channel can reach twice the volume of droplets in a dry channel. The volume of slugs formed with no gas flow ($Q_G = 0$) for pre-wetted and dry channel walls have been drawn as dashed horizontal lines in Fig. 6; these values bound the slug volumes derived from sessile and pendant droplets in the presence of gas flow. This is strong evidence that shear forces from the gas flow play a minor role in liquid droplet growth and slug formation.

5.3. Pressure drop at the droplet-to-slug transition

Fig. 8 shows the bridge pressure Δp_1 as a function of gas and liquid flow rates, and of pore orientation. The water droplets grow in the channel creating a narrow gap between the liquid and the

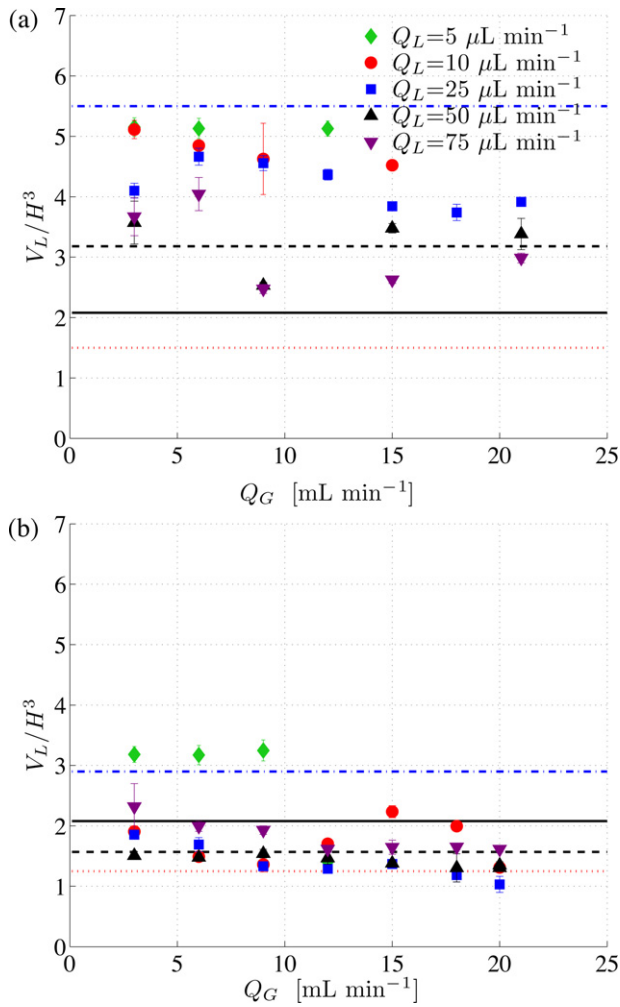


Fig. 6. Dimensionless removed (water) volume V_L/H^3 vs. Q_G . (a) Sessile slugs. (b) Pendant slugs. Markers: mean values experimentally observed. The lines represent analytical estimates (Eqs. (4) and (5)) for $\theta_s = 70^\circ$ in three cases; (1) black (solid) line: $Bo = 0$ (no gravity field) and; (2–3) black (dashed) lines: $Bo = \pm 0.34$. Red (dotted) line: experimental value observed with no gas flow $Q_G = 0$ on a “dry” channel. Blue (dot-dashed) line: experimental value for $Q_G = 0$ on a “wet” channel. (For interpretation of the references to color in this figure legend, the reader is referred to the web version of this article.)

opposing wall. As the gap narrows, the pressure drop associated with the gas flow increases. The water droplet can grow longitudinally, which also increases the pressure drop for gas flow. The bridge pressure for sessile droplets ranges between 30 and 60 Pa (see Fig. 8a); there is no apparent correlation between the bridge pressure and gas or liquid flow rates. Pendant droplets have a much broader range of bridge pressure; the bridge pressure varies between 10 and 80 Pa (see Fig. 8b). There is a weak correlation between the bridge pressure and gas flow rate for pendant droplets.

5.4. Pressure drop for slug motion

The water droplet that forms is pinned with its receding edge at the liquid pore. After water droplets completely span the gas flow channel, the differential gas pressure increases to a high value; the liquid slug detaches from its pinned location and moves down the channel. The gas pressure drop remains high, decreasing slightly as the slug moves (see Fig. 4a). The slug moves at the nominal gas speed, $U = Q_G/H^2$. The mean pressure drop for slug motion, Δp_2 , is reported in Fig. 9 as a function of gas/liquid flow rates and pore orientation. The differential pressure for slug motion ranges between

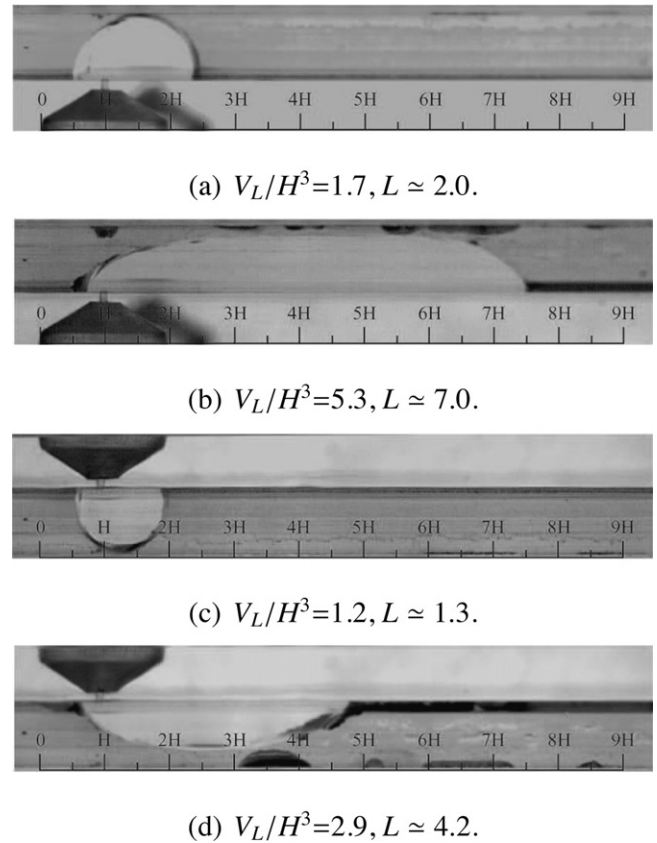


Fig. 7. No gas flow ($Q_G = 0$, $Q_L = 10 \mu\text{L min}^{-1}$). Droplets that bridge vertically and laterally at different wetting conditions. The scale indicates the slug length L in units of the channel height. (a) Sessile droplet (pore facing up) on a “dry” channel. (b) Sessile droplet on a wet substrate. (c) Pendant droplet (pore facing down) on a “dry” substrate. (d) Pendant droplet on a wet substrate.

200 and 250 Pa; it is independent of the pore orientation and there is no evidence for any correlation with liquid flow rate Q_L . There is a small increase of the differential pressure with increasing gas flow rates. Previous studies of slug flow in square channels [26] reported that the pressure drop for slug motion increases with the capillary number $Ca_L = U\mu_L/\gamma$ to the two-thirds power. Our experimental data is consistent with these reports.

6. Discussion and analysis: predictive model development

The experimental study presented here focuses on understanding how droplets and slugs form in the gas flow channels of PEM fuel cells. A precisely located emergent liquid pore in a transparent gas channel provides a well-defined geometry for direct observation and quantification of the forces involved in slug formation and detachment.

A number of previous studies have also used video imaging to identify flow regimes in fuel-cell channels [8,9,13]. Those studies reported flow regime maps that correlated different flow patterns such as slugs, films, and mist flows as functions of the superficial gas speed U_G and liquid speed U_L . Several of those studies [8] employed porous gas diffusion layers where the water emerged from a couple of different points randomly located in the flow channel. In those studies, slug flow was typically observed at low gas speeds $U_G < 1 \text{ m s}^{-1}$ for a range of liquid speeds ($10^{-5} \lesssim U_L \lesssim 10^{-4} \text{ m s}^{-1}$) where the gas-to-liquid volumetric ratio is small ($Q = U_G/U_L \lesssim 10^{-4}$). Multiple flow patterns (e.g. slugs, films, mist flows) were observed at high gas speed for a given liquid speed.

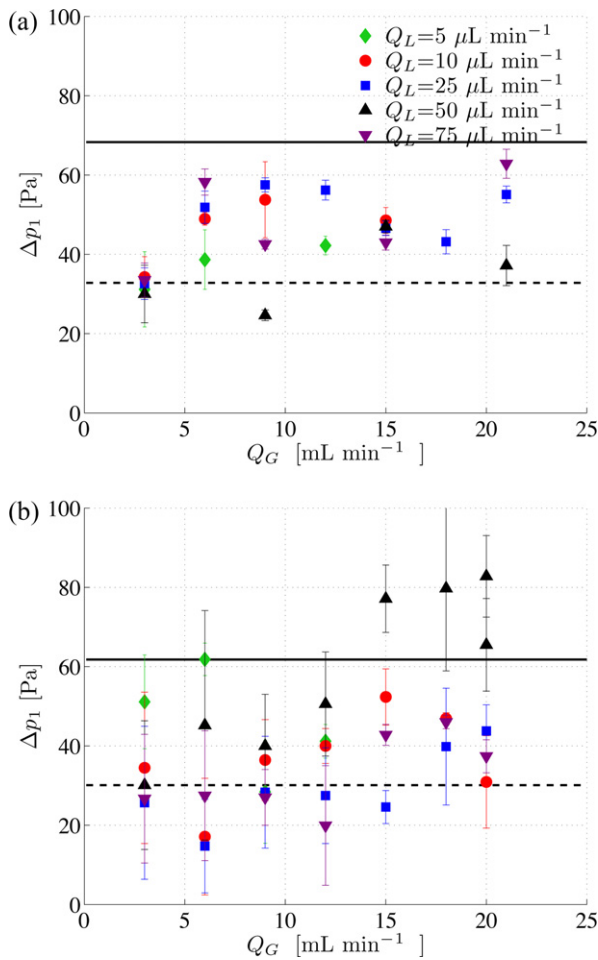


Fig. 8. Pressure drop $\Delta p_1 = p_1 - p_{out}$ at the droplet-to-slug transition vs. gas flow rate Q_G . (a) Sessile droplet. (b) Pendant droplet. Solid (black) line: analytical estimate (Eqs. (11) and (12)) for $\theta_T = 45^\circ$. Dashed (black) line: analytical estimate (Eqs. (11) and (12)) for $\theta_T = 70^\circ$.

In this initial study we focused on the growth of emergent droplets, their conversion into slugs, and the subsequent motion of single slugs in horizontal gas flow channels. The key results are:

1. Droplets grow with their receding contact line pinned at the pore. The droplets first grow to span the gas flow channel from side to side and then grow longitudinally while remaining laterally confined.
2. At a critical length the confined droplets completely span the cross section of the gas flow channel; the upstream gas pressure increases and causes the droplets to form slugs that detach and move down the channel at a speed $U = Q_G/H^2$.
3. The slugs move with an apparent advancing contact angle of $\sim 90^\circ$ and an apparent receding contact angle of $\sim 0^\circ$.
4. Slug volumes are weakly dependent on liquid and gas flow rates.
5. The slug volumes formed from pendant droplets are smaller than those formed from sessile droplets.
6. In the absence of gas flow, slug volumes are smaller in channels with dry surfaces than in channels with pre-wetted surfaces.
7. The pressure to detach and move water slugs is weakly dependent on the gas and liquid flow rates, and the emergent pore orientation with respect to gravity.

The most obvious conclusion from these results is that under laminar flow conditions ($\rho_G U_G H / \mu_G < 100$), the shear forces that the gas flow exerts on the liquid droplets are of secondary importance

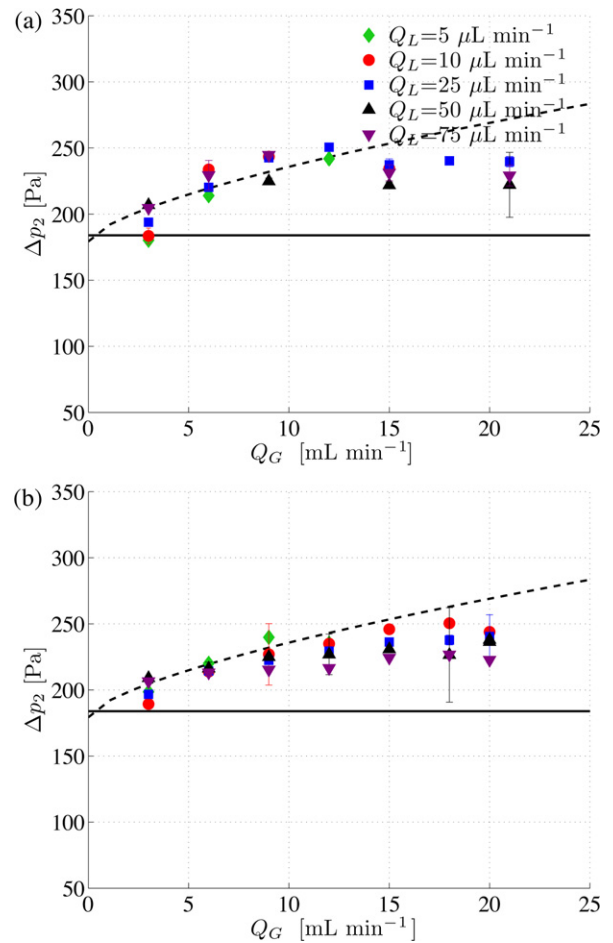


Fig. 9. Pressure drop $\Delta p_2 = p_2 - p_{out}$ during slug flow vs. gas flow rate Q_G . (a) Sessile droplet. (b) Pendant droplet. Solid (black) line: single-value approximation $\Delta p_2 = 4p_{cap}$. Dashed (black) line: two-thirds power law in experimental fit $\Delta p_2 = (3.9 + 130 Ca_L^{2/3})p_{cap}$ where $Ca_L = U\mu_L/\gamma$.

in the formation of droplets and slugs. The corollary conclusion is that gravity and interfacial forces are the dominant forces that determine the volume of slugs and the energy required to remove them.

6.1. Force balances in confined gas–liquid flows

The relative importance of viscous, interfacial, and gravity forces associated with droplet and slug formation and motion can be quantified in terms of dimensionless groups. Since this is a two-phase flow, the dimensionless groups must be appropriately defined. The key groups are the Reynolds number, Bond number, and capillary numbers.

1. $Re_G = \rho_G U_G H / \mu_G = 2-25$ corresponds to laminar flow, where the gas–liquid interface is smooth; water is only transported as films or slugs. At high Re_G (e.g. $Re_G > 2000$), turbulence at the gas–liquid interface may result in mist flow.
2. $Bo = \rho_L g H^2 / \gamma = 0.34$. The Bond number is the ratio of gravity to interfacial forces. For $Bo \sim \mathcal{O}(1)$ the two forces are approximately equal and gravity may be expected to alter the droplet formation.
3. The capillary number is the ratio of viscous to interfacial forces. We encounter three versions of the capillary number corresponding to (i) the ratio of the shear forces of the flowing gas to the interfacial forces at the (advancing/receding) contact line of the droplet, $Ca_G = U\mu_G/\gamma \sim 10^{-5}$; (ii) the ratio of the shear forces

of the flowing gas to the interfacial forces connecting the droplet to the liquid inside the pore, Ca_p defined in Section 6.2; (iii) the ratio of the shear forces between the moving liquid slug and the wall to the interfacial forces at the (advancing/receding) contact line of the moving slug, $Ca_L = U\mu_L/\gamma \sim 10^{-3}$. The small value of all three capillary numbers indicates that viscous forces are small compared to the interfacial forces, except near the droplet-to-slug transition as elaborated in Section 6.2.

6.2. Effects of the pore on droplet growth and slug detachment

The ratio of the viscous forces that the gas exerts on the droplet to the adhesion force between the droplet and the liquid in the pore is given by the modified capillary number

$$Ca_p = Ca_G \left(\frac{H}{d}\right) \left(\frac{H}{h_{gap}}\right)^2 \quad (3)$$

where $h_{gap} = H - h$ is the gap thickness through which the gas flows and h is the droplet height. This modified capillary number rescales the gas-based capillary number by the ratios of channel height to the pore diameter ($H/d \simeq 10$) and channel height to the gap thickness (Hh^{-1}_{gap}). The capillary number $Ca_G \sim 10^{-5}$ is very small. Only when the gap thickness becomes small, i.e. $h_{gap} \lesssim 0.01H$, does $Ca_p \sim \mathcal{O}(1)$ and viscous shear forces become sufficient to detach a droplet. Adhesion of the droplet to the liquid inside the pore keeps the droplet pinned, allowing its growth until it laterally spans the flow channel. Even with hydrophobic gas diffusion electrodes, the emergent droplet can still remain pinned on the electrode surface because of adhesion to the liquid column inside the pore.

In fuel cells, the sizes of pores and their locations are randomly distributed. This makes it difficult to predict and control where water droplets and slugs will form. Kimball et al. [27] showed that it is possible to prescribe the location of the emergent liquid by creating $250 \mu\text{m}$ pores at specific positions in the gas diffusion layer. Prescribing the location of the emergent liquid into the gas flow channel results in a system that is analogous to the present experimental setup.

6.3. Slug volumes

Slug volumes can be predicted based on a simple analytical model. The photo sequence in Fig. 4b–d shows that water emerges from the pore and initially forms a nearly cylindrical cap. Neglecting the droplet curvature in the transverse yz -plane the volume can be approximated by standard formula for a cylindrical cap

$$V_L = h^3 \frac{\theta - (1/2) \sin(2\theta)}{(1 - \cos \theta)^2} \quad (4)$$

where θ is the apparent contact angle observed from the side and h is the droplet height at the apex. The slug volume is estimated from the volume of a fully confined droplet given by Eq. (4) with $h = H$. The error associated with neglecting the transverse curvature is discussed in Section 6.5.

The liquid droplet shape is altered by gravity and gas flow. As reported in Fig. 4b–d, and elaborated later in Section 6.5, the gas pressure drop is substantially smaller than the Laplace (or capillary) pressure $\Delta p_G \ll p_{cap}$ for laterally confined droplets when $h \lesssim 0.9H$. Therefore, effects of the external gas pressure may be neglected in the present model. Gravity compresses a sessile droplet decreasing the apparent contact angle. Gravity pulls on a pendant droplet increasing the apparent contact angle. The apparent contact angle may be estimated from a force balance in the xy -plane between the Laplace pressure determined by the longitudinal local curvature

and the hydrostatic pressure determined by gravity. The apparent contact angle θ is related to the static contact angle θ_S by

$$\cos \theta = \cos \theta_S \pm Bo \quad (5)$$

where $Bo = \rho_L g H^2 / \gamma$ is the Bond number previously defined and the \pm corresponds to the case of a sessile/pendant droplet. Slug volumes can be roughly estimated through Eqs. (4) and (5) by assuming that the droplet-to-slug transition occurs when the apex of the cylindrical cap reaches the opposite channel wall. Such estimates were obtained assuming a square channel and $\theta_S = 70^\circ$ for three cases (see Fig. 6): (1) no gravity; (2) sessile droplets; and (3) pendant droplets. The model prediction without gravity falls between the experimental values obtained for sessile and pendant droplets. Including gravity in the model predicts that the apparent contact angle decreases for sessile droplets, increasing slug volumes; the apparent contact angle increases for pendant droplets, reducing slug volumes. Volumes predicted by Eqs. (4) and (5) match the experimental data for sessile droplets within 35% and for pendant droplets within 15%. Large day-to-day fluctuations observed in the slug volumes are largely due to a random distribution of residual water in the flow channel. In light of the probabilistic nature of the observed phenomena, the developed model provides adequate estimations for preliminary design purposes.

6.4. The effect of residual water on the droplet-to-slug transition

We observed that residual micro-droplets and films are left behind by moving slugs. Those residual micro-droplets can act as nucleating sites for subsequent droplet-to-slug transitions. The effect of residual water on the transition of a sessile droplet into a slug is captured in the video sequence shown in Fig. 10. A water micro-droplet is located at the top-right corner downstream of the growing droplet; the micro-droplet is shown circled in the top and side views of Fig. 10. The rapid conversion into a slug is triggered when the advancing interface of the fully confined droplet touches the residual micro-droplet. The images in Fig. 10 are 5 ms apart, showing how fast the transition occurs. In both side and top views in Fig. 10 one can see capillary waves and a wetting front moving from the residual droplet location toward the pore. The moving contact lines dividing wet and non-wet surfaces are clearly seen in the top images of Fig. 10b. The additional feature observed in the side images is the change in curvature at both the receding and advancing interfaces. After the slug is pushed down the channel, another residual micro-droplet is left behind at approximately the same location; this results in a reproducible sequence, giving rise to successive slugs of similar volume.

6.5. Pressure at the droplet-to-slug transition

A confined droplet adopts two radii of curvature as illustrated in Fig. 5c and d; R is the radius of curvature in the longitudinal xy -plane while r is the transverse radius of curvature in the yz -plane. When a fully confined droplet forms, as seen in Figs. 5d and 10, a gap of thickness $h_{gap} \ll H$ and length $L_{gap} \sim V_L/H^2$ develops along the central section of the droplet through which gas can flow. The upstream gas pressure is $p_{in} = p_{out} + \Delta p_G$ and the downstream gas pressure is p_{out} . The pressure drop across the droplet scales with the gas flow rate and gap length $\Delta p_G \propto Q_G L_{gap}$. Inside the droplet, however, the hydrostatic pressure at a given height ($y = \text{const.}$) remains approximately constant $p_L \sim \text{const.}$ (the pressure drop due to the small liquid flow $\sim Q_L/H^2$ is negligible). This means that the local pressure jump across the gas–liquid interface must decrease along the gap as must the local transverse curvature of the droplet surface. For a perfectly smooth and dry channel surface, one would expect the rapid conversion into a slug at a critical gap length where the

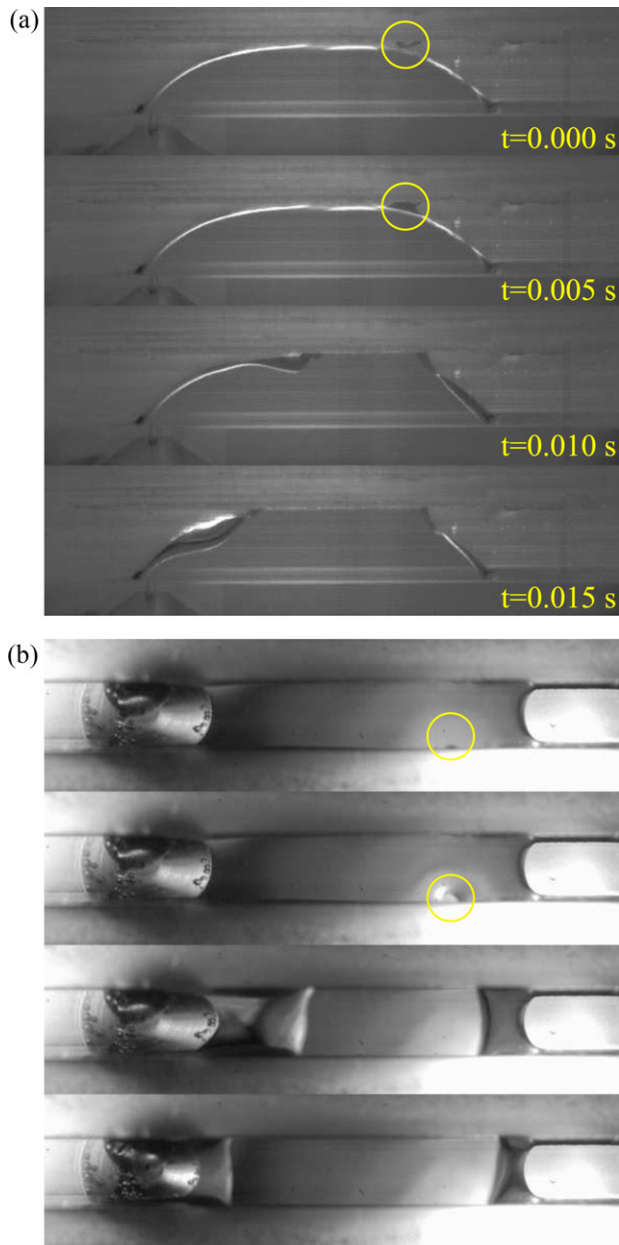


Fig. 10. High-speed video taken at 2000 fps shows micro-droplet coalescence and contact-line nucleation. The images in the two sequences are 0.005 s apart. (a) Side view. (b) Top view.

pressure drop Δp_G is large enough so that the transverse curvature $1/r \rightarrow 0$ and the gap thickness $h_{gap} \rightarrow 0$.

In vertical confinement the droplet, at its apex, plateaus longitudinally ($R \rightarrow \infty$) while the transverse radius of curvature is

$$r = \frac{H}{2 \cos \theta_T}, \quad (6)$$

and the maximum gap thickness is

$$h_{gap}(\theta_T) \simeq \frac{H(1 - \sin \theta_T)}{2 \cos \theta_T}. \quad (7)$$

Both r and h_{gap} given by Eqs. (6) and (7) are determined solely by an apparent (transverse) contact angle θ_T . The upstream liquid pressure is

$$p_L^u = p_{out} + \Delta p_G \pm \rho_L g(H - h_{gap}(\theta_T^u)) - \frac{2\gamma \cos \theta_T^u}{H} \quad (8)$$

Table 3

Pressure drop Δp_G and gap length L_{gap} at the droplet-slug transition as predicted by Eqs. (11) and (12) for $Ca_G = 3.3 \times 10^{-5}$.

θ_T ($^\circ$)	h_{gap}/H	Δp_G (Pa)	L_{gap}/H
70 (sessile)	0.09	32.8	4.9
70 (pendant)	0.09	30.1	4.5
45 (sessile)	0.23	68.3	131.9
45 (pendant)	0.23	61.8	119.4

and the downstream liquid pressure is

$$p_L^d = p_{out} \pm \rho_L g(H - h_{gap}(\theta_T^d)) - \frac{2\gamma \cos \theta_T^d}{H}. \quad (9)$$

Both pressures in the liquid are measured at the droplet base ($y=0$). In Eqs. (8) and (9) the apparent contact angles θ_T^u and θ_T^d correspond to the values of the gap thickness at the upstream and downstream ends. Since the liquid inside the droplet is nearly at rest then $p_L^u = p_L^d$; subtracting Eqs. (8) and (9) leads to

$$\frac{\Delta p_G}{p_{cap}} \pm Bo \left(\frac{h_{gap}(\theta_T^d) - h_{gap}(\theta_T^u)}{H} \right) + 2(\cos \theta_T^d - \cos \theta_T^u) = 0. \quad (10)$$

The droplet-to-slug transition occurs when $\theta_T^d = 90^\circ$ and thus $h_{gap}(\theta_T^d) = 0$ at the downstream end; Eq. (10) simplifies to

$$\frac{\Delta p_G}{p_{cap}} = 2 \cos \theta_T^u \pm Bo \frac{h_{gap}(\theta_T^u)}{H}. \quad (11)$$

Eq. (11) predicts the gas pressure drop at the droplet-to-slug transition (i.e. the bridge pressure); this bridge pressure is determined by the transverse contact angle θ_T^u upstream of the gap and by the pore orientation.

The slug size can be estimated from the critical gap length L_{gap} associated with the gas pressure drop Δp_G at bridging. Based on lubrication theory [28] the critical gap length is

$$\frac{L_{gap}}{H} = \frac{\Delta p_G}{p_{cap}} \frac{1}{3Ca_G} \left(\frac{h_{gap}(\theta_T^u)}{H} \right)^3. \quad (12)$$

Predicted critical gap lengths based on Eqs. (11) and (12) are summarized in Table 3 for the maximum gas flow rate employed in the experiments. Assuming an apparent contact angle $\theta_T = 70^\circ$, the gap thickness is $h_{gap}/H = 0.09$, the bridge pressure is $\Delta p_G \simeq 30$ Pa, and the critical gap length is $L_{gap} \simeq 4\text{--}5H$. These values are in reasonable agreement with experimental observations reported in Figs. 6 and 8. Because the gap thickness is small, the volume of the gap $V_{gap} \simeq 0.05V_L$ is only 5% of the slug volume; this validates the two-dimensional approximation employed in Section 6.3. If the contact angle is reduced to $\theta_T = 45^\circ$, Eqs. (11) and (12) predict larger gap thickness $h_{gap}/H = 0.23$, gap volumes $V_{gap} \simeq 0.15V_L$, and bridge pressures $\Delta p_G \simeq 60\text{--}70$ Pa. However, the length of the critical gap length $L_{gap} \simeq 120H$ is significantly longer than the slug lengths (V_L/H^2) observed in these experiments. We believe this is further evidence of the role of residual water micro-droplets acting as nucleation sites for the droplet-to-slug transition.

6.6. Anomalous slug lengths and film formation

Under steady flow conditions we always observed slugs with sizes that are within the range of values predicted by Eqs. (4) and (5); the slug volumes depended primarily on interfacial forces, gravity, and channel dimensions. The slug volumes resulting from sessile droplets were $3\text{--}5 H^3$ while those derived from pendant droplets were $1\text{--}2 H^3$. However, during start-up with a dry channel the sessile slugs were much larger than those seen at “steady” state. In the extreme, at the lowest liquid flow rates and highest gas flow rates studied, the first sessile droplets spanned the entire length

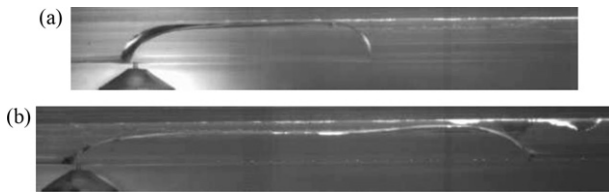


Fig. 11. Thick films observed after the channel surface undergoes extensive drying: (a) anomalously long droplet under high gas flow rate $Q_G = 20 \text{ mL min}^{-1}$ and low liquid flow rate $Q_L = 10 \mu\text{L min}^{-1}$, (b) Thick liquid film spreads under high gas and liquid flow rates $Q_G = 20 \text{ mL min}^{-1}$, $Q_L = 50 \mu\text{L min}^{-1}$.

of the channel ($V > 64H^3$). Over time the length of the sessile slugs decreased, eventually reaching the steady state volumes reported in Fig. 6. The initial sessile slug volume decreased with increasing liquid flow, but the initial slug volume was always greater than the steady-state slug volumes.

The initial pendant slugs formed in dry channels were also larger than their steady-state counterparts. Nevertheless, pendant slugs were always much smaller than sessile slugs. Furthermore, the time to reach steady state was faster for pendant slugs than for sessile slugs.

Examples of anomalously long sessile droplets and thick films that formed during start-up are shown in Fig. 11 for low and high liquid flow rates. At the lower liquid flow rate the first sessile droplet could grow to span the entire length of the channel. At higher liquid flow rates, the sessile droplet elongated forming a thick film that may break to form slugs before spanning the entire channel length. As described in the previous section, the elongation is possible because of a lubrication pressure that develops in the gas layer between the droplet and the opposing wall. When the channel is dry, the transverse curvature prevents the sessile droplets from wetting the top surface of the channel. After the channel corners become wet, the residual water micro-droplets can nucleate a wetting front for the droplet-to-slug transition.

Sessile droplet lengths are limited by either the advancing liquid encountering a nucleation site for the droplet-to-slug transition, or the gas pressure drop Δp_G causing the transverse curvature to vanish at the downstream end of the gap. Either of these conditions leads to the formation of a slug by allowing the droplet to wet the opposing wall of the channel. The simple geometric model presented in Section 6.3 works well for predicting slug volumes at “steady” state because the droplet elongation is limited by the presence of residual micro-droplets.

Spreading of sessile water droplets along the length of the channel can have a deleterious effect on fuel cell operation. Kimball et al. [27] showed that if sessile droplets formed near the inlet of the gas flow channel during fuel cell start-up, the droplet elongated longitudinally forming a liquid film over the entire length of the gas diffusion layer. This film blocked oxygen or air from reaching the cathode catalyst layer.

6.7. Pressure drop for slug motion

Once droplets become slugs, the gas flow is blocked and the upstream gas pressure increases. When the pressure is sufficiently large it causes the slugs to detach. The pressure drop required for liquid slug motion must overcome the interfacial forces to advance the slug contact lines, as well as the viscous drag for gas and liquid flow.

The data presented in Fig. 9 shows that the pressure drop for slug motion had a dominant component that was independent of gas flow and gravity. There was a minor component of the pressure drop that increased with the gas flow. The pressure drop was

primarily due to interfacial forces with a lesser contribution from viscous forces; gravity is irrelevant for horizontal slug flow.

The force balance between the pressure exerted by the gas and the interfacial forces at the receding/advancing contact lines is given by the following equation

$$\Delta p_2 H^2 = 4H\gamma(\cos \theta_R - \cos \theta_A). \quad (13)$$

Direct observation of the slug motion is illustrated in Fig. 4h and i. The advancing contact angle was $\sim 90^\circ$ and the receding contact angle was $\sim 0^\circ$ which predicts a pressure drop of $4p_{cap} = 185 \text{ Pa}$. This value is approximately 75% of the maximum pressure drops reported in Fig. 9. In addition, there are contributions to the pressure drop due to dynamic changes in the advancing contact angle and viscous dissipation in the receding film which increase with the capillary number $Ca_L = Q_G \mu_L / \gamma H^2$. Previous analyses of slug flow in square channels reported a pressure drop $\Delta p_2 = (p_{th} + K Ca_L^{2/3}) p_{cap}$ [26]. A best-fit curve to the data using this two-thirds power scaling, valid for $Ca_L \ll 1$, is shown in Fig. 9 where the $p_{th} = 3.9$ is the threshold interfacial force and $K \sim 32.5$ is an adjustable parameter. Above a critical value of the capillary number (i.e. for high gas flow rate $Q_G \gtrsim 15 \text{ mL min}^{-1}$) a correction to the two-thirds power law [29] that accounts for the finite thickness of the receding liquid film can provide a better fit to the experimental data. This topic, of particular interest to slug flow in gas-liquid systems, will be treated in a future communication.

7. Implications for fuel cell design

We introduced a systematic approach using a well-defined geometry to quantitatively analyze a specific flow regime that is of critical importance for PEM fuel cell operation. This work is the first in a series of studies where the present approach will be applied to analyze other flow regimes. By elucidating the physics of how droplets emerge and form slugs in the gas flow channels we obtained analytical predictions. This approach can assist in the rational design of flow channels for fuel cells. Specific results of importance are:

1. The work to remove slugs is primarily controlled by the wetted perimeter of the gas flow channel. It requires less energy removing the same liquid volume in a single (large) slug than removing it through multiple (smaller) slugs.
2. Hydrophobic materials for the gas flow channels should reduce the slug volumes, which would require more work to remove the same volume of water. However, the smaller slugs may improve mass transport from the gas flow channel to the catalyst layer.
3. Water adhesion to the corners of gas flow channels can cause large differences in slug volumes between start-up and steady-state operation of PEM fuel cells.
4. Fuel cells with the cathode facing upwards with respect to gravity are susceptible to forming liquid films that could cover the GDL surface and permit gas bypass through the cathode flow channel without reaction.

Further examination of different flow regimes, channel orientations, surface properties, and flow geometries are still needed to fully develop quantitative models. With the working model developed in this study, we are able to quantitatively predict the removed water volumes and pressure required for their removal. These data maybe employed to compare the fuel cell efficiency of different flow field designs.

8. Conclusions

This paper has refined the use of *ex situ* studies to elucidate how water emerging from pores of a porous fuel cell electrode would form droplets and slugs in the gas flow channels of a PEM fuel cell. The experiments demonstrated that the geometry of the flow channel and interfacial forces were the dominant factors that determined the size of slugs and the work required to remove liquid water. Specifically the experiments showed:

1. Emergent liquid pores pin the droplets to locations where the droplets can grow until they span the channel to form slugs and detach.
Interfacial forces and geometry are the dominant factors that determine the volumes of emerging droplets and formed slugs in the gas flow channels.
2. Gravity is important in the force balance that determines when droplets span the flow channel and form slugs. Slugs formed from pendant droplets are smaller than slugs formed from sessile droplets.
3. The wetting properties of the channel walls are altered by residual water that accumulates particularly at the corners of square channels.
4. At start-up with dry channels, sessile droplets are pinned at the corners of the channel and grow to be anomalously long. At steady-state operation, the volumes of the formed slugs become smaller due to the presence of residual water. Residual water droplets left by previous slugs act as nucleating agents for the droplet-to-slug transition.
5. We presented simple analytical models that predict slug volumes and pressure drops. We were able to obtain acceptable quantitative agreement with experiments that include the effects of gravity and gas flow.

Experimental results demonstrated that residual water in the form of micro-droplets and thin films play a major role in the dynamics of slug formation and detachment. Numerical studies will need to incorporate such experimentally observed features to accurately model the conditions in the gas flow channel during PEM fuel cell operation.

Acknowledgements

We gratefully acknowledge M. Roche and the Complex Fluids Group at Princeton directed by H.A. Stone, L. Roquemore and R.

Maqueda from the Princeton Plasma Physics Laboratory (PPPL), for their technical assistance and equipment loan. We acknowledge E. Afotey, J. Badwick, and Q. Duan for their help conducting experiments related to the present work. We thank the National Science Foundation (CBET-0754715) and Department of Energy (DE-SC-0002097) for partial support of this work. M.J. Cheah also thanks the Princeton University Program in Plasma Science and Technology for partial support under U.S. Department of Energy contract No. DE-AC02-76-CHO-3073.

References

- [1] M. Mench, in: Fuel Cell Engines, John Wiley & Sons, Inc, 2008.
- [2] C. Yang, S. Srinivasan, A. Bocarsly, S. Tulyani, J. Benziger, J. Membr. Sci. 237 (1–2) (2004) 145–161.
- [3] F. Weng, A. Su, C. Hsu, C. Lee, J. Power Sources 157 (2) (2006) 674–680.
- [4] X. Liu, H. Guo, C. Ma, J. Power Sources 156 (2) (2006) 267–280.
- [5] Z. Lu, S. Kandlikar, C. Rath, M. Grimm, W. Domigan, A. White, M. Hardbarger, J. Owejan, T. Trabold, Int. J. Hydrogen Energy 34 (8) (2009) 3445–3456.
- [6] D. Wilkinson, H. Voss, K. Prater, J. Power Sources 49 (1–3) (1994) 117–127.
- [7] K. Tüber, D. Pócza, C. Hebling, J. Power Sources 124 (2) (2003) 403–414.
- [8] R. Anderson, L. Zhang, Y. Ding, M. Blanco, X. Bi, D. Wilkinson, J. Power Sources 195 (15) (2010) 4531–4553.
- [9] I. Hussaini, C. Wang, J. Power Sources 187 (2) (2009) 444–451.
- [10] M. Hickner, N. Siegel, K. Chen, D. Hussey, D. Jacobson, M. Arif, J. Electrochem. Soc. 155 (2008) B294.
- [11] D. Spemjak, A. Prasad, S. Advani, J. Power Sources 170 (2) (2007) 334–344.
- [12] T. Trabold, J. Owejan, D. Jacobson, M. Arif, P. Huffman, Int. J. Heat Mass Transfer 49 (25–26) (2006) 4712–4720.
- [13] F. Zhang, X. Yang, C. Wang, J. Electrochem. Soc. 153 (2006) A225.
- [14] Z. Lu, C. Rath, G. Zhang, S. Kandlikar, Int. J. Hydrogen Energy 36 (16) (2011) 9864–9875.
- [15] A. Bazylak, D. Sinton, N. Djilali, J. Power Sources 176 (1) (2008) 240–246.
- [16] A. Theodorakakos, T. Ous, M. Gavaises, J. Nouri, N. Nikolopoulos, H. Yanagihara, J. Colloid Interface Sci. 300 (2) (2006) 673–687.
- [17] J. Steinbrenner, E. Lee, C. Hidrovo, J. Eaton, K. Goodson, J. Power Sources 196 (11) (2011).
- [18] T. Trabold, Heat Transfer Eng. 26 (3) (2005) 3–12.
- [19] L. Zhang, H. Bi, D. Wilkinson, J. Stumper, H. Wang, J. Power Sources 183 (2) (2008) 643–650.
- [20] X. Liu, H. Guo, F. Ye, C. Ma, Electrochim. Acta 52 (11) (2007) 3607–3614.
- [21] N. Akhtar, A. Qureshi, J. Scholta, C. Hartnig, M. Messerschmidt, W. Lehnert, Int. J. Hydrogen Energy 34 (7) (2009) 3104–3111.
- [22] K. Chen, M. Hickner, D. Noble, Int. J. Energy Res. 29 (12) (2005) 1113–1132.
- [23] X. Zhu, P. Sui, N. Djilali, J. Power Sources 181 (1) (2008) 101–115.
- [24] J. Benziger, J. Nehlsen, D. Blackwell, T. Brennan, J. Itescu, J. Membr. Sci. 261 (1–2) (2005) 98–106.
- [25] E. Kimball, T. Whitaker, Y. Kevrekidis, J. Benziger, AIChE J. 54 (5) (2008) 1313–1332.
- [26] C. Ody, Microfluid. Nanofluid. 9 (2) (2010) 397–410.
- [27] E. Kimball, J. Benziger, Y. Kevrekidis, Fuel Cells 10 (4) (2010) 530–544.
- [28] G. Batchelor, in: An Introduction to Fluid Dynamics, Cambridge Univ. Press, 2000.
- [29] P. Aussillous, D. Quéré, Phys. Fluids 12 (10) (2000) 2367–2371.